# Suzaku Observations of Thermal and Non-Thermal X-Ray Emission from the Middle-Aged Supernova Remnant G156.2+5.7

Satoru Katsuda[1,2], Robert Petre[1], Una Hwang[1], Hiroya Yamaguchi[3], Koji Mori[4], and Hiroshi Tsunemi[2]

*Satoru.Katsuda@nasa.gov, Robert.Petre-1@nasa.gov, Una.Hwang-1@nasa.gov, hiroya@crab.riken.jp, mori@astro.miyazaki-u.ac.jp, tsunemi@ess.sci.osaka-u.ac.jp*

[1]*NASA Goddard Space Flight Center, Greenbelt, MD 20771, U.S.A.*

[2]*Department of Earth and Space Science, Graduate School of Science, Osaka University, 1-1 Machikaneyama, Toyonaka, Osaka 560-0043, Japan*

[3]*RIKEN (The Institute of Physical and Chemical Research), 2-1 Hirosawa, Wako, Saitama 351-0198*

[4]*Department of Applied Physics, Faculty of Engineering, University of Miyazaki, 889-2192, Japan*

## Abstract

We present results from X-ray analysis of a Galactic middle-aged supernova remnant (SNR) G156.2+5.7 which is bright and largely extended in X-ray wavelengths, showing a clear circular shape (radius$\sim$50$'$). Using the Suzaku satellite, we observed this SNR in three pointings; partially covering the northwestern (NW) rim, the eastern (E) rim, and the central portion of this SNR. In the NW rim and the central portion, we confirm that the X-ray spectra consist of soft and hard-tail emission, while in the E rim we find no significant hard-tail emission. The soft emission is well fitted by either a one-component or two-component non-equilibrium ionization (NEI) model. In the NW and E rims, a one-component (the swept-up interstellar medium) NEI model well represents the soft emission. On the other hand, in the central portion, a two-component (the interstellar medium and the metal-rich ejecta) NEI model fits the soft emission better than the one-component NEI model from a statistical point of view. The relative abundances in the ejecta component suggest that G156.2+5.7 is a remnant from a core-collapse SN explosion whose progenitor mass is less than $15\,M_\odot$. The origin of the hard-tail emission detected in the NW rim and the central portion of the SNR is highly likely non-thermal synchrotron emission from relativistic electrons. In the NW rim, the relativistic electrons seems to be accelerated by a forward shock with a slow velocity of $\sim$500$\,$km$\,$sec$^{-1}$.

**Key words:** ISM: abundances – ISM: individual (G156.2+5.7) – ISM: supernova

remnants – X-rays: ISM

## 1. Introduction

G156.2+5.7 is a large (radius$\sim$50$'$), X-ray bright supernova remnant (SNR) discovered by the ROSAT all-sky survey (Pfeffermann et al. 1991). The ROSAT 0.1–2.4 keV band spectrum was well represented by emission from a thin thermal plasma with a temperature of about 0.5 keV. A Sedov analysis based on the X-ray data showed a very low density medium of $0.01\,\mathrm{cm}^{-3}$, an age of $\sim$26000 yr, and a distance to the remnant of $\sim$3 kpc.

Subsequently, successful X-ray observations were performed with Ginga and ASCA. Using non-imaging instruments on board Ginga, Yamauchi et al. (1993) found that the scan profile in the 1.2–3 keV energy band was similar to the soft X-ray image observed with ROSAT, while the scan profile above 3 keV revealed two bumps near to the north and south edges of the remnant. ASCA observed the northern and central portions of the remnant (Yamauchi et al. 1999). ASCA spectra from both north and central portions were characterized by soft and hard-tail components. The soft component was dominated by line emission, and originated from non-equilibrium ionization (NEI) plasma. A revised Sedov analysis based on the spectral parameters determined by the soft component resulted in a low ambient density of $\sim$0.2 $\mathrm{cm}^{-3}$, an age of $\sim$15000 yr, and a distance of $\sim$1.3 kpc. On the other hand, the hard-tail component was most likely represented by a power-law type spectrum, i.e., synchrotron emission from relativistic electrons.

The distance to G156.2+5.7 has not yet been established. Gerardy & Fesen (2007) discovered considerable faint H$\alpha$ line emission coincident with X-ray emission. Since some of them seems to be associated with interstellar clouds located at a distance of 0.3 kpc, they argued that the distance to the remnant might be closer than that was estimated previously. We here take 1 kpc as a distance to the remnant, following the most recent paper on G156.2+5.7 (Xu et al. 2007).

Radio observations show a bilateral shell structure having relatively weak emission at the central portion of the remnant (Reich et al. 1992). Although the radio surface brightness was the lowest among all known SNRs, a magnetic field in the shell was estimated to be 16 $\mu$G (at a distance of 1 kpc) which is just slightly higher than a typical interstellar magnetic field. Therefore, Reich et al. (1992) concluded that the low surface brightness was due to the low ambient density. Polarized radio emission shows a nearly perfect tangential magnetic field configuration along the shell, which is typical for evolved shell-type SNRs (Reich et al. 1992; Xu et al. 2007). All the observations agree that G156.2+5.7 is a middle-aged SNR whose SN explosion occurred in a low-density ambient medium.

We focus on both thermal and non-thermal X-ray emission in this SNR, using the most
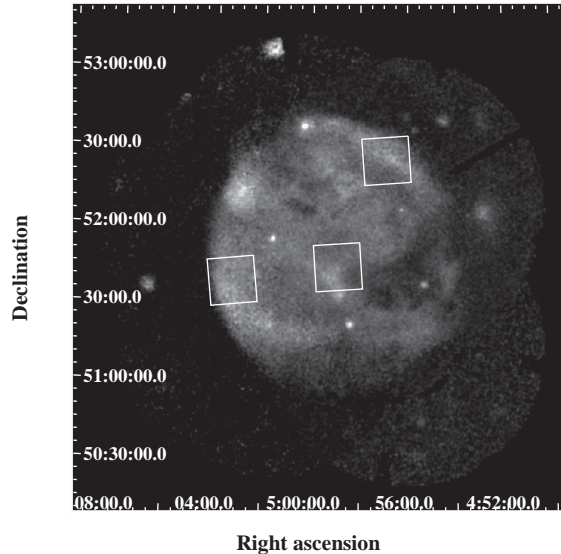
**Fig. 1.** ROSAT PSPC image of the entire G156.2+5.7. The energy range is 0.05–3.0 keV. The effects of vignetting and exposure are corrected. The image is binned by $15''$ and is smoothed by a Gaussian kernel of $\sigma = 45''$. The intensity scale is square root. The Suzaku/XIS FOV ($17'.8 \times 17'.8$) are shown as white boxes.

recent X-ray astronomy satellite Suzaku (Mitsuda et al. 2007). The fact that non-thermal X-ray emission is detected from this middle-aged SNR is very interesting, since a currently accepted theory of diffusive shock acceleration requires high shock velocity of at least $\sim 2000\,\mathrm{km\,sec^{-1}}$ which is not expected in middle-aged SNRs to produce non-thermal emission in the X-ray domain. Fortunately, the thermal emission from this SNR allows us to investigate ambient medium densities as well as the shock velocities which are important to study the theory of diffusive shock acceleration. Another interesting aspect of this remnant is a clear evidence of Si and S rich ejecta detected in the central portion of the remnant with ASCA (Yamauchi et al. 1999). We can investigate the progenitor star which produced this SNR, by comparing the relative metal abundances of the ejecta with those expected in nucleosynthetic models.

## 2. Observations and Data Screening

We observed the eastern (E) rim, the northwestern (NW) rim, and the central portion of G156.2+5.7 during 2007 February 16–20 with the Suzaku satellite. We here concentrate on the data taken by the X-ray Imaging Spectrometer (XIS; Koyama et al. 2007) onboard Suzaku. The XIS consists of two front-illuminated (FI; XIS0 and XIS3) CCD cameras and one back-illuminated (BI; XIS1) CCD camera. Each camera covers an identical imaging area of $17'.8 \times 17'.8$. The fields of view (FOV) of XIS for the three observations are shown as white boxes in the entire X-ray image of the SNR obtained by the ROSAT PSPC (figure 1). We reprocessed the XIS data, using the latest CTI calibration file of version 20080131. We cleaned the repro-
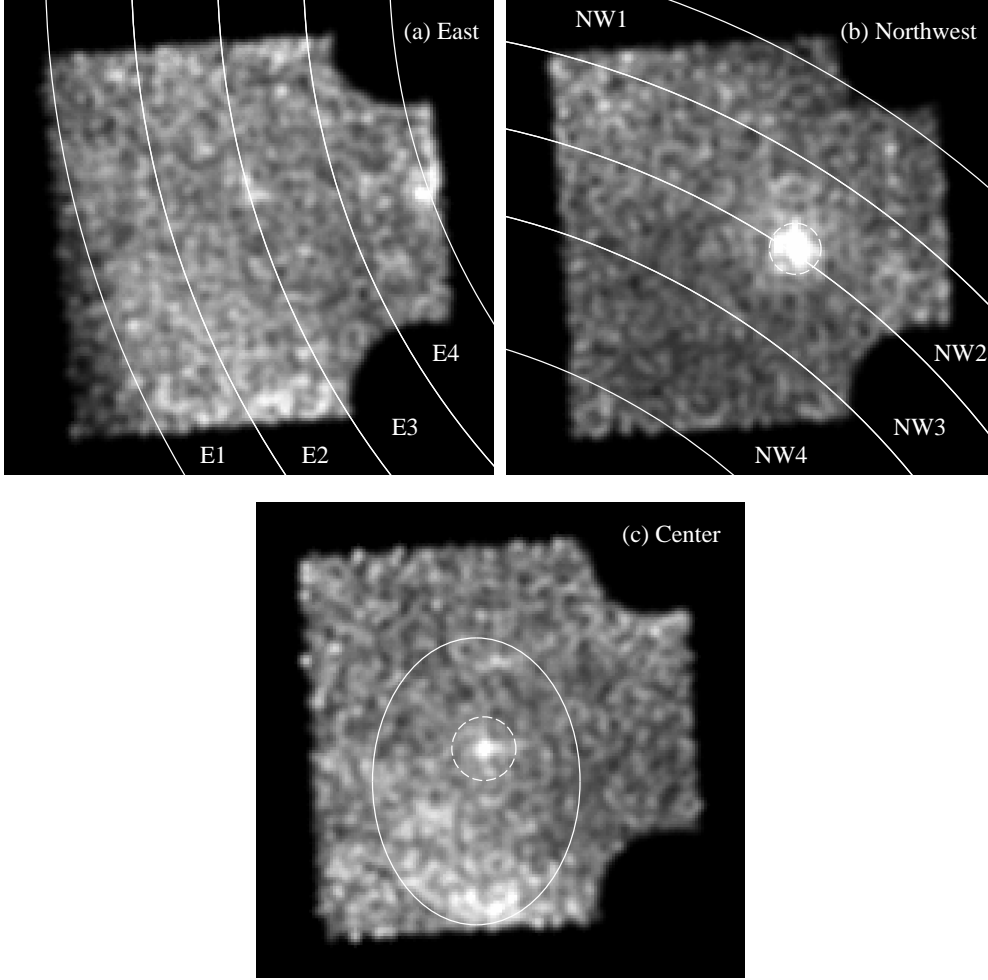
**Fig. 2.** NXB-subtracted Suzaku XIS0 images of the three pointings. The energy range is 0.4–8.0 keV. The effects of exposure, vignetting, and contamination are corrected. The image is binned by $8''$ and is smoothed by a Gaussian kernel of $\sigma = 24''$. The intensity scale is square root. White curves are the regions where we extract spectra. We exclude two point sources enclosed by dashed circles from our spectral analyses.

cessed data by the standard criteria[1] recommended by the calibration team of Suzaku/XIS. After the screening, the remaining exposure times were 53.3 ks for the E rim, 50.5 ksec for the NW rim, and 51.2 ksec for the central portion, respectively.

Figure 2 shows the vignetting-corrected XIS0 images of the three observations. Two corners of each FOV where the calibration source of $^{55}$Fe is illuminated are masked in these images.

---

[1] See the Suzaku Data Reduction Manual which can be found from http://heasarc.gsfc.nasa.gov/docs/suzaku/analysis/abc.
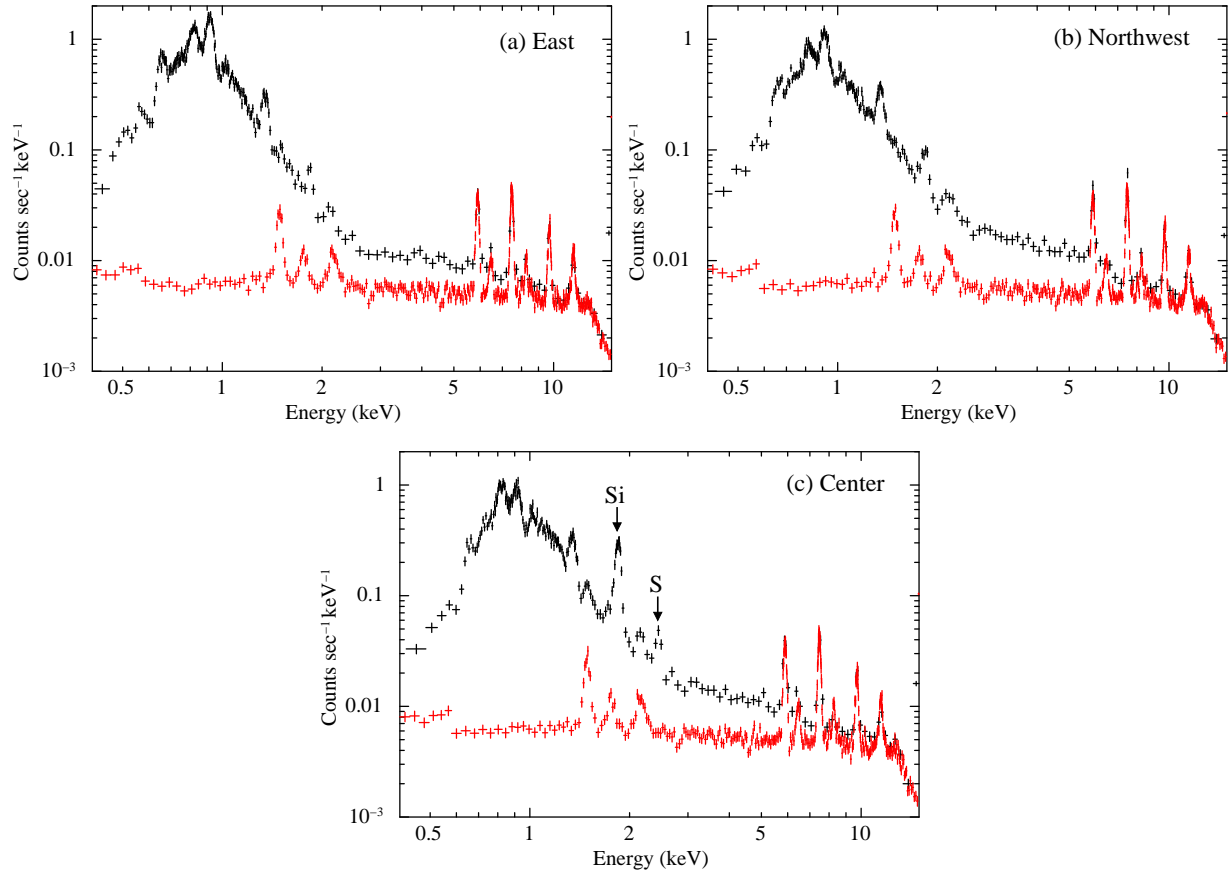
**Fig. 3.** XIS0 spectra from the entire FOV (black crosses). (a), (b), and (c) are responsible for the E rim, the NW rim, and the central portion, respectively. Non X-ray background spectra are also shown as red crosses.

## 3.  Spectral Analysis and Results

Figure 3 shows XIS0 spectra extracted from the entire FOV for each observation. The non X-ray background (NXB; see the next subsection for an explanation) spectra are also shown as red crosses. The signal-to-noise (black-to-red in figure 3) ratios in an energy band of 3–5 keV significantly vary among the three FOV, indicating a non-uniformity of the hard-tail emission detected by Ginga and ASCA (Yamauchi et al. 1993; 1999). Also notable is a variation of equivalent widths of K-shell lines from Si (at $\sim$1.85 keV) and S (at $\sim$2.4 keV); those in the central spectrum are much larger than those in the rim spectra. This implies the existence of the fossil ejecta in the central portion as was detected with ASCA (Yamauchi et al. 1999). In the following spectral fitting procedure, we use photons in the energy range of 0.4–8.0 keV, and employ the XSPEC (version 12.4.0) software.

## 3.1. Background

As background, we consider three kinds of sources; NXB caused by charged particles and $\gamma$-rays hitting the detectors, cosmic X-ray background (CXB) which accounts for emission from unresolved point sources, and local hot bubble (LHB) that is a hot gas surrounding the earth. Note that Galactic ridge X-ray emission (GRXE) is negligible for this SNR; based on literature by Sugizaki et al. (2001) and Revnivtsev et al. (2006), we estimate the flux of GRXE at the Galactic longitude, $l$, $l = 100°$ within Galactic latitudes, $b$, $|b| < 1°$ to be $4 \times 10^{-16}$ erg cm$^{-2}$ sec$^{-1}$ arcmin$^{-2}$ in a range of 0.7–10 keV, which is about 0.3 % of that from G156.2+5.7 (Yamauchi et al. 1999). Furthermore, the larger values of $l(= 156.2)$ and $b(= 5.7)$ for this SNR would prefer the smaller flux of GRXE. We generate NXB spectra suitable for our observations, by employing `xisnxbgen` provided by the XIS team (Tawa et al. 2008). The generated NXB spectra are shown in figure 3, in which we can see that the NXB spectra above 8 keV, where emission from astrophysical sources is negligible, match the data. Therefore, we are confident that NXB emission is properly subtracted by the NXB spectra generated by `xisnxbgen`. We subtract NXB emission from the same area as the source area in detector coordinates. For the CXB emission, we employ broken power-law model with photon indices $\Gamma$ ($<0.7$ keV) $= 2.0$ and $\Gamma$ ($>0.7$ keV) $= 1.4$ (e.g., Miller et al. 2008). As for the LHB component, we use the APEC model (Smith et al. 2001) with solar composition (Anders & Grevesse 1989) and an electron temperature of 0.1 keV (e.g., Tawa 2008). We estimate the emission measure of the LHB component around G156.2+5.7 to be $2 \times 10^{-3}$ pc cm$^{-6}$, based on the surface brightness in the ROSAT PSPC R1 and R2 bands of $\sim 2.8$ counts sec$^{-1}$ arcmin$^{-2}$. We exclude two point-like sources visible in our FOV from our spectral analyses; the regions excluded are enclosed by dashed circles as shown in Fig. 2.

## 3.2. E Rim

We perform annular spectral analyses for the E and NW rims. We choose the center of the X-ray SNR at position (RA, DEC)=($4^h59^m05^s$, $51°50'57''$) [J2000] determined by a ROSAT PSPC surface brightness contour. For the E rim, the annular regions are spaced by $4'$ from a radial position, r $= 48'$ to r $= 32'$, resulting in four annular regions (from E1 at the outermost region to E4 at the innermost region). These annular regions are shown in figure 2 as white curves.

We perform spectral fittings for the NXB-subtracted spectra. Since previous ASCA observations showed non-equilibrium ionization (NEI) states in this SNR, we apply an absorbed NEI model (VNEI model [e.g., Borkowski et al. 2001]) having LHB and CXB components for all the four spectra. The free parameters are the hydrogen column density, $N_H$; electron temperature, $kT_e$; the ionization timescale, $\tau$ ($\tau$ is the product of the electron density multiplied by the time after the shock heating); the emission measure, EM (EM$= \int n_e n_H dl$, where $n_e$ and $n_H$ are the number densities of electrons and protons, respectively and $dl$ is the plasma depth);

abundances of N, O, Ne, Mg, Si, S, and Fe. The other elemental abundances are assumed to the solar values (Anders & Grevesse 1989), since emission lines from these elements cannot be seen in the Suzaku spectra. We first allow the normalization of the CXB component to vary. We then find that the mean flux of the CXB component derived in the four annular regions is $4.7 \times 10^{-15}$ erg cm$^{-2}$ sec$^{-1}$ arcmin$^{-2}$ in 2.0–10.0 keV. This is consistent with the CXB flux of $4.4 \times 10^{-15}$ erg cm$^{-2}$ sec$^{-1}$ arcmin$^{-2}$ estimated by blank sky observations with Suzaku (Tawa 2008). Since the CXB flux fluctuates by about 10% from location to location, we take the mean CXB flux derived in the four annular regions as a local flux around this SNR. After fixing the normalization of the CXB to the mean flux, we fit all the spectra with a one-component VNEI model. This model gives us fairly good fits for all the spectra; the reduced-$\chi^2$ values (d.o.f.) range from 1.04 (753) to 1.27 (837). No additional power-law component for possible hard-tail emission is required at a 99% confidence level. Therefore, we consider that this model well represents the spectra in the E rim. We use this CXB flux value in the following analysis. Figure 4 (a) shows the example spectrum (from E3) with the best-fit model. The best-fit parameters for the four spectra are listed in Table 1.

We find that the values of $kT_e$ significantly decreases toward the shock front from 0.44 keV to 0.28 keV. This trend is generally seen either in Sedov-phase SNRs or behind the shock fronts interacting with dense interstellar medium (ISM) (e.g., Miyata & Tsunemi 1999; Levenson et al. 2005; Hwang et al. 2005). The measured abundances are almost constant in the FOV. The typical abundance of 0.5 times the solar value is consistent with those derived in the northern rim of this SNR obtained with ASCA (Yamauchi et al. 1999). The sub solar abundance leads us to consider that the origin of the plasma in the E rim is the ISM swept-up by the forward shock. We should note that the N abundance is depleted to at least 0.1 times the solar value which is not expected in the ISM plasma. In our data, it is quite difficult to establish whether or not this strong depletion is real, given the fact that we do not know the composition of contaminants built up on the optical blocking filters of the XIS (Koyama et al. 2007) in addition to weak N emission lines from G156.2+5.7. The value of $N_H$ is almost constant in the FOV, and is consistent with those derived by the ASCA observations (Yamauchi et al. 1999).

## 3.3. NW Rim

In the NW rim, we also extract four spectra from annular regions (from NW1 at the outermost region to NW4 at the innermost region). The width of the innermost region is 6′, while those of the other regions are 4′. These annular regions cover from r = 30′ to r = 48′, and are shown in figure 2 as white curves. We first apply the same model as we used for the spectral modeling in the E rim, i.e., a one-component VNEI model for the emission from G156.2+5.7. This model gives us an acceptable fit for the innermost region (NW4). Therefore, we consider this model as the best-representative model for the NW4 region. The
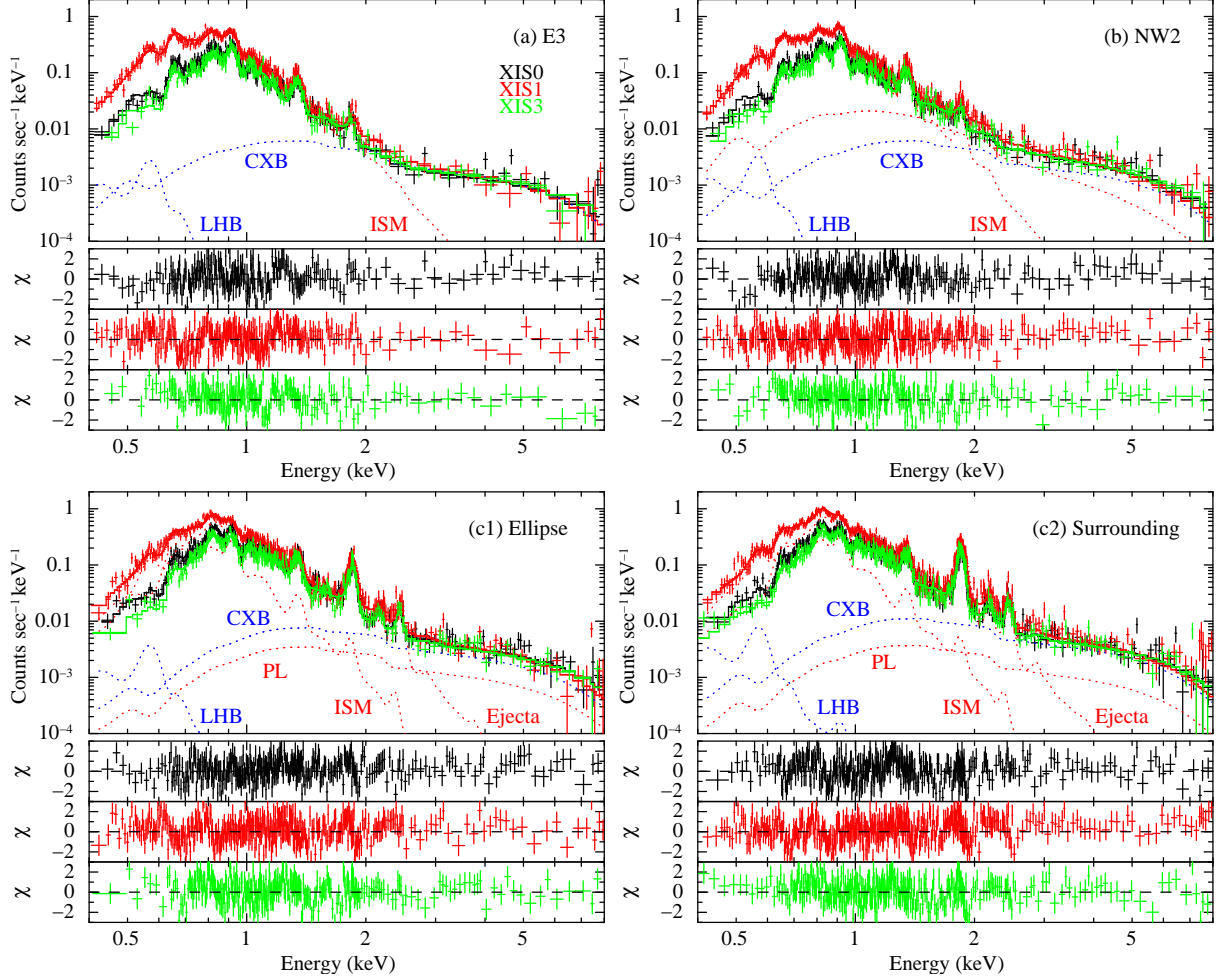
**Fig. 4.** Example spectra with their best-fit models. The best-fit curves are shown as solid lines (total components) or dotted lines (individual components). The lower panels show the residuals. The spectral extraction regions are (a) from E3 in figure 2 (a), (b) from NW2 in figure 2 (b), and (c1) or (c2) from the ellipse region or the surrounding region in figure 2 (c).

best-fit parameters are listed in Table 1. On the other hand, the fit levels for the other three spectra are not acceptable; we see excess emission from the best-fit models above 3 keV. This is at least qualitatively consistent with the fact that Yamauchi et al. (1999) detected hard-tail emission above 3 keV in the ASCA spectra. Therefore, we add either a thermal (NEI) or a power-law component for the hard-tail emission. We set metal abundances of the additional NEI component to 0.5 times the solar value which is a typical abundance of the ISM around G156.2+5.7. The $kT_e$, $\tau$, and EM for the additional NEI component, or photon index and normalization for the additional power-law component are treated as free parameters. Both VNEI+NEI and VNEI+power-law model dramatically improve the fits for all the three spectra; e.g., the value of $\chi^2$/d.o.f. for the NW2 region is reduced from 1240/911 to 1065/909. The example spectrum with the best-fit VNEI+power-law model for the NW3 region is shown in

**Table 1.** Spectral-fit parameters for the E and/or NW rim.

| Parameter | E1 | E2 | E3 | E4 | NW4 |
|---|---|---|---|---|---|
| $N_{\rm H}[\times 10^{21}{\rm cm}^{-2}]$ .. | 3.7±0.1 | 3.2±0.1 | 2.5±0.1 | 3.4±0.1 | 4.1±0.1 |
| $kT_{\rm e}$[keV] ......... | 0.28±0.01 | 0.35±0.01 | 0.45±0.01 | 0.44±0.01 | 0.51±0.01 |
| N ................ | 0.11±0.05 | <0.06 | <0.02 | <0.03 | <0.04 |
| O ................ | 0.38±0.01 | 0.43±0.01 | 0.38±0.01 | 0.32±0.01 | 0.32±0.02 |
| Ne .............. | 0.68±0.02 | 0.69±0.02 | 0.60±0.02 | 0.40±0.02 | 0.43±0.03 |
| Mg ............. | 0.57±0.05 | 0.57±0.01 | 0.49±0.04 | 0.32±0.04 | 0.41±0.04 |
| Si ............... | 0.8±0.2 | 0.5±0.1 | 0.5±0.1 | 0.4±0.1 | 0.9±0.1 |
| S ............... | <1 | <0.5 | <1 | <0.7 | 1.0±0.7 |
| Fe .............. | 0.45±0.02 | 0.51±0.01 | 0.46±0.02 | 0.34±0.02 | 0.38±0.02 |
| $\log(\tau/{\rm cm}^{-3}\,{\rm sec})$... | 10.96±0.03 | 10.80±0.03 | 10.62±0.03 | 10.50±0.03 | 10.53±0.04 |
| EM[†][$\times 10^{18}$ cm$^{-5}$]. | 3.26±0.07 | 1.63±0.03 | 0.72±0.02 | 1.22±0.04 | 0.74±0.02 |
| Surface brightness[§] | $3.0\times10^{-13}$ | $2.4\times10^{-13}$ | $1.3\times10^{-13}$ | $1.9\times10^{-13}$ | $1.3\times10^{-13}$ |
| $\chi^2$/d.o.f. ......... | 781/753 | 1065/837 | 886/763 | 684/569 | 632/603 |

[*]Other elements are fixed to those of solar values.

The values of abundances are multiples of solar value.

The errors are in the range $\Delta\chi^2 < 2.7$ on one parameter.

[†]EM denotes the emission measure $\int n_{\rm e}n_{\rm H}dl$.

[§]In unit of erg cm$^{-2}$ sec$^{-1}$ arcmin$^{-2}$ in a range of 0.5–10 keV.

figure 4 (b). The best-fit parameters for the three spectra are shown in Table 2.

The surface brightness of the hard-tail component, $\sim 5\times 10^{-15}$ erg cm$^{-2}$ sec$^{-1}$ arcmin$^{-2}$, is consistent with that detected with ASCA/GIS in the northern portion of the remnant (Yamauchi et al. 1999). We find that the VNEI+power-law model fits the data slightly better than the VNEI+NEI model. However, it is not very safe to exclude the possibility of the VNEI+NEI model (i.e., the thermal origin for the hard-tail emission) from a statistical point of view. Thus, we consider about astrophysical aspects. If thermal origin is the case, the high $kT_{\rm e}$ of above 3 keV suggests that G156.2+5.7 is as young as historical young SNRs. As already pointed out by Gerardy & Fesen (2007), this is unlikely, since there have been no historical record of the SN explosion toward G156.2+5.7. Furthermore, the spatial variation of $kT_{\rm e}$, i.e., the value of $kT_{\rm e}$ is at least two times higher at the outermost region than those in the inner regions (see, Table 2), conflicts what we expect behind shock fronts; $kT_{\rm e}$ generally decreases toward the shock front due to deceleration of the shock as well as the effect of thermal non-equilibration between ions and electrons. On the other hand, if non-thermal origin is the case, the spectral flattening towards the outer region (see, Table 2) is consistent with that seen at the rim of Tycho's SNR (Cassam-Cheinaï et al. 2007). Therefore, we believe that the origin of the hard-tail emission is non-thermal emission rather than thermal emission.

The abundances derived by the VNEI component responsible for the soft emission from G156.2+5.7 are similar to those observed in the E rim, suggesting that the origin of the plasma in the NW rim is also the swept-up ISM. The values of $kT_e$ are also similar to those in the E rim. This fact implies similar forward shock velocities in both the NW rim and the E rim.

## 3.4. Center

We extract two spectra in the central FOV. One is a central ellipse region, where we can see enhanced surface brightness relative to the surrounding region in the ROSAT PSPC image (see, figure 1), the other is the rest of the FOV. We first apply the same one-component VNEI model as we did for the E rim spectra. Then, we obtain the reduced-$\chi^2$ values (d.o.f.) for the central ellipse and the surrounding region to be 1.33 (1103) and 1.38 (1334), respectively. Taking into consideration that systematic uncertainties of the response, the fit level might be acceptable from statistical point of view. However, apparent excess emission in the hard energy band (above 3 keV) is found. Therefore, we add either an NEI or a power-law component for the hard-tail emission. The best-fit parameters are shown in Table 2. Although the additional component (either NEI or power-law) significantly improves the fits for both spectra (reduced-$\chi^2$ values are 1.25 for the ellipse region and 1.34 for the surrounding region), we still see obvious discrepancy between our data and the best-fit models around 0.5–0.6 keV (He-like O K$\alpha$ line) and 1.2–1.3 keV (Fe L). This means that the VNEI+(NEI or power-law) model is too simple to reproduce the soft (thermal) emission from G156.2+5.7.

Since Yamauchi et al. (1999) found metal-rich ejecta at the central portion of the SNR, it is reasonable to consider that at least two kinds of plasmas (the swept-up ISM and the metal-rich ejecta) exist along the line of sight at the center of the SNR. We thus apply a two-component (ISM and ejecta component) VNEI model to represent the thermal emission from G156.2+5.7. Assuming that abundances of the ISM are uniform around G156.2+5.7, we set abundances of the ISM component to the typical values derived in the E or NW rims (N=0.05, O=0.4, Ne=0.6, Mg=0.5, Si=0.6, S=0.6, and Fe=0.5 × the solar values, and the other metals are assumed to be the solar values). In order to reduce the number of free parameters and obtain meaningful results, we also set the value of $kT_e$ for the ISM component to 0.3 keV that is typical for the outermost regions in the E and NW rim. The $kT_e$ for the ejecta component is left as a free parameter. The $\tau$ and EM are left as free parameters for both ISM and ejecta components. We also left the metal abundances of O, Ne, Mg, Si, S, and Fe for the ejecta component as free parameters. Since it is quite difficult to constrain the abundance of N due to poor statistics below 0.5 keV for the ejecta component, we set the abundance of N to be equal to that of O. In this way, we apply the 2VNEI+(NEI or power-law) model for the two spectra extracted in the central FOV. This model significantly improves the fits. The best-fit parameters are listed in Table 3. The example spectrum from the surrounding region is shown in figure 4 (c). Since this model gives us nearly acceptable fits for both spectra and there is no

10

**Table 2.** Spectral-fit parameters for the NW rim and the central portion.

| Component | Parameter | NW1 | NW2 | NW3 | Ellipse | Surrounding |
|---|---|---|---|---|---|---|
| | | Model: VNEI+NEI | | | | |
| Absorption | $N_H[\times10^{21}\mathrm{cm}^{-2}]$ ... | 3.7±0.1 | 3.3±0.1 | 3.9±0.1 | 4.1±0.1 | 3.9±0.1 |
| VNEI | $kT_e[\mathrm{keV}]$ ......... | 0.32±0.01 | 0.40±0.01 | 0.43±0.01 | 0.46±0.01 | 0.52±0.01 |
| | N ............... | <0.03 | <0.01 | <0.02 | <0.02 | <0.01 |
| | O ............... | 0.34±0.02 | 0.35±0.01 | 0.32±0.02 | 0.32±0.01 | 0.28±0.01 |
| | Ne .............. | 0.52±0.02 | 0.65±0.02 | 0.50±0.02 | 0.39±0.02 | 0.44±0.02 |
| | Mg .............. | 0.44±0.05 | 0.63±0.04 | 0.46±0.03 | 0.37±0.02 | 0.46±0.03 |
| | Si ............... | 0.6±0.2 | 0.7±0.1 | 0.6±0.1 | 2.1±0.1 | 3.0±0.1 |
| | S ............... | <0.8 | <0.4 | <1.2 | 1.7±0.4 | 3.8±0.6 |
| | Fe ............... | 0.37±0.02 | 0.47±0.02 | 0.38±0.01 | 0.50±0.01 | 0.59±0.01 |
| | $\log(\tau/\mathrm{cm}^{-3}\mathrm{sec})$.... | 10.82±0.04 | 10.70±0.03 | 10.64±0.04 | 10.56±0.02 | 10.71±0.02 |
| | $EM^\dagger[\times10^{18}\mathrm{cm}^{-5}]$ .. | 2.03±0.06 | 1.14±0.02 | 1.17±0.03 | 1.21±0.02 | 0.63±0.01 |
| | Surface brightness$^\S$ | $2.3\times10^{-13}$ | $1.7\times10^{-13}$ | $1.7\times10^{-13}$ | $2.1\times10^{-13}$ | $1.1\times10^{-13}$ |
| NEI | $kT_e[\mathrm{keV}]$ ......... | >7 | $3.2^{+0.4}_{-0.5}$ | 3.4±0.6 | $6^{+4}_{-2}$ | >5 |
| | Metal abundance . | 0.5 (fixed) | 0.5 (fixed) | 0.5 (fixed) | 0.5 (fixed) | 0.5 (fixed) |
| | $\log(\tau/\mathrm{cm}^{-3}\mathrm{sec})$.... | >12 | >12 | >12 | >12 | >12 |
| | $EM^\dagger[\times10^{18}\,\mathrm{cm}^{-5}]$ . | 0.030±0.005 | 0.06±0.01 | 0.053±0.006 | 0.027±0.004 | 0.014±0.003 |
| | Surface brightness$^\S$ | $3.7\times10^{-15}$ | $5.2\times10^{-15}$ | $4.8\times10^{-15}$ | $3.1\times10^{-15}$ | $1.8\times10^{-15}$ |
| $\chi^2$/d.o.f. ........................ | | 676/588 | 1065/909 | 981/796 | 1375/1101 | 1796/1332 |
| | | Model: VNEI+power-law | | | | |
| Absorption | $N_H[\times10^{21}\mathrm{cm}^{-2}]$ ... | 3.9±0.1 | 3.4±0.1 | 3.9±0.1 | 4.0±0.1 | 3.9±0.1 |
| VNEI | $kT_e[\mathrm{keV}]$ ......... | 0.31±0.01 | 0.37±0.01 | 0.43±0.01 | 0.48±0.01 | 0.50±0.01 |
| | N ............... | <0.04 | <0.02 | <0.04 | <0.03 | <0.03 |
| | O ............... | 0.36±0.02 | 0.43±0.02 | 0.40±0.02 | 0.36±0.01 | 0.38±0.02 |
| | Ne .............. | 0.53±0.02 | 0.85±0.03 | 0.66±0.03 | 0.46±0.02 | 0.64±0.03 |
| | Mg .............. | 0.44±0.05 | 0.80±0.05 | 0.59±0.05 | 0.44±0.03 | 0.64±0.04 |
| | Si ............... | 0.5±0.2 | 0.8±0.2 | 0.8±0.1 | 2.4±0.1 | 4.2±0.2 |
| | S ............... | <1 | <0.7 | <2 | 2.1±0.5 | 5.9±0.8 |
| | Fe ............... | 0.37±0.02 | 0.60±0.02 | 0.49±0.02 | 0.58±0.01 | 0.80±0.02 |
| | $\log(\tau/\mathrm{cm}^{-3}\mathrm{sec})$.... | 10.84±0.04 | 10.79±0.03 | 10.67±0.04 | 10.58±0.02 | 10.74±0.02 |
| | $EM^\dagger[\times10^{18}\,\mathrm{cm}^{-5}]$ . | 2.25±0.06 | 1.05±0.02 | 0.90±0.02 | 1.00±0.02 | 0.49±0.01 |
| | Surface brightness$^\S$ | $2.3\times10^{-13}$ | $1.8\times10^{-13}$ | $1.6\times10^{-13}$ | $2.0\times10^{-13}$ | $1.1\times10^{-13}$ |
| Power-law | Photon Index...... | $1.7^{+0.2}_{-0.1}$ | $2.9^{+0.1}_{-0.9}$ | 2.6±0.1 | 2.3±0.1 | 2.6±0.2 |
| | Norm$^\ddagger$ ........... | 7±1 | 38±3 | 27±2 | 13±2 | 13±2 |
| | Surface brightness$^\S$ | $3.9\times10^{-15}$ | $9.9\times10^{-15}$ | $7.9\times10^{-15}$ | $4.5\times10^{-15}$ | $3.5\times10^{-15}$ |
| $\chi^2$/d.o.f. ........................ | | 674/589 | 1036/909 | 954/796 | 1375/1101 | 1781/1332 |

$^*$Other elements are fixed to those of solar values.

The values of abundances are multiples of solar value.

The errors are in the range $\Delta\chi^2 < 2.7$ on one parameter.

$^\dagger$EM denotes the emission measure $\int n_e n_H dl$.

strong reason to add further components, we stop introducing additional components.

If we assume that the hard-tail component is represented by the thermal model, the value of $kT_e$ is measured to be unreasonably high (above $\sim6\,\mathrm{keV}$). Therefore, we consider that the hard-tail emission is most likely explained by the power-law type spectrum rather than the thermal spectrum. The metal abundances for the ejecta component are indeed higher than the solar values, confirming that it originates from the metal-rich ejecta. The abundances in the ejecta component are significantly different between the central ellipse and the surrounding region; the abundances for the central ellipse are all lower than those for the surrounding region. The relatively low abundances at the central ellipse might be caused by either a mixing of the ISM into the ejecta component or technical difficulty in separating the ISM component and the ejecta component.

## 4.  Discussion

We detected line-dominated soft emission in all the three pointings i.e., the E rim, the NW rim, and the central portion of this SNR. In the E and NW rims, the spectra of the soft emission show similar shapes, and are represented by thermal emission originating from the swept-up ISM. On the other hand, in the central portion, the spectra of the soft emission show an additional component corresponding to metal-rich ejecta. In addition to the soft emission, we detected hard-tail emission in the NW rim and the central portion. The origin of this hard-tail emission is more consistent with non-thermal synchrotron emission rather than thermal emission.

### 4.1.  Thermal Emission

Our annular analyses for the rim regions revealed spatial variation of spectral parameters. The $kT_e$ decreases from the innermost region ($\sim0.5\,\mathrm{keV}$) toward the shock front ($\sim0.3\,\mathrm{keV}$), while the EM increases toward the shock front. These trends are at least qualitatively consistent with those expected in the Sedov-phase SNRs. Then, we compare the EM profiles obtained in the E and NW rims with those derived from a simple Sedov solution, to derive physical parameters as well as to check whether or not they are well explained by a simple Sedov solution. Varying the value of the ambient density and calculating $\chi^2$-values, we search for the most suitable (best-fit) ambient densities to represent the EM profiles for the E rim and the NW rim, respectively. Figure 5 shows the EM profiles obtained in the E (data points with circles) and the NW (data points with triangles) rims as well as the best-fit EM profiles (solid line for the E rim and dashed line for the NW rim, respectively) as a function of radius. The best-fit pre-shock ambient densities for the E and NW rims are derived to be 0.091 and 0.084 cm$^{-3}$, respectively. These values are consistent with previous results based on X-ray observations (0.01–0.2 cm$^{-3}$). Looking at figure 5, we see apparent deviations at the outermost regions for both the E and NW rims; the data exceed the best-fit models by factors of $\sim1.8$ (E) or $\sim1.4$

**Table 3.** Spectral-fit parameters for the central ellipse and the surrounding region in the central FOV.

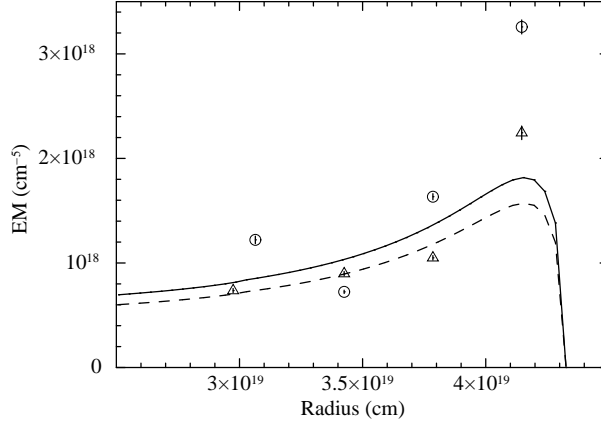| Component | Parameter | Ellipse | Surrounding |
|---|---|---|---|
| | Model: 2VNEIs+NEI | | |
| Absorption | $N_{\rm H}[\times10^{21}{\rm cm}^{-2}]$ ... | 4.3±0.1 | 4.6±0.1 |
| VNEI (ISM) | $kT_{\rm e}$[keV] ......... | 0.3 (fixed) | 0.3 (fixed) |
| | $\log(\tau/{\rm cm}^{-3}\,{\rm sec})$.... | 10.46±0.05 | $10.64^{+0.06}_{-0.05}$ |
| | EM[†]$[\times10^{18}{\rm cm}^{-5}]$.. | 1.09±0.05 | 0.95±0.03 |
| | Surface brightness[§] | $1.3\times10^{-13}$ | $1.1\times10^{-13}$ |
| VNEI (ejecta) | $kT_{\rm e}$[keV] ......... | 0.48±0.01 | 0.54±0.01 |
| | O(=N) .......... | 0.48±0.04 | 2.8±0.3 |
| | Ne .............. | 0.25±0.03 | 0.9±0.1 |
| | Mg ............. | 0.40±0.03 | 1.5±0.1 |
| | Si .............. | 1.8±0.1 | 9.5±0.4 |
| | S .............. | 3.1±0.6 | 10±1 |
| | Fe .............. | 0.66±0.02 | 2.6±0.07 |
| | $\log(\tau/{\rm cm}^{-3}\,{\rm sec})$.... | 11.08±0.03 | 11.30±0.02 |
| | EM[†]$[\times10^{18}{\rm cm}^{-5}]$.. | 0.76±0.02 | 0.149±0.003 |
| | Surface brightness[§] | $1.2\times10^{-13}$ | $0.74\times10^{-13}$ |
| NEI | $kT_{\rm e}$[keV] ......... | >7 | >6 |
| | Metal abundance . | 0.5 (fixed) | 0.5 (fixed) |
| | $\log(\tau/{\rm cm}^{-3}\,{\rm sec})$.... | >12 | >12 |
| | EM[†]$[\times10^{18}\ {\rm cm}^{-5}]$ . | 0.021±0.004 | 0.014±0.003 |
| | Surface brightness[§] | $2.7\times10^{-15}$ | $1.8\times10^{-15}$ |
| $\chi^2$/d.o.f............................ | | 1281/1100 | 1596/1331 |
| | Model: 2VNEIs+power-law | | |
| Absorption | $N_{\rm H}[\times10^{21}{\rm cm}^{-2}]$ ... | 4.2±0.1 | 4.2±0.1 |
| VNEI (ISM) | $kT_{\rm e}$[keV] ......... | 0.3 (fixed) | 0.3 (fixed) |
| | $\log(\tau/{\rm cm}^{-3}\,{\rm sec})$.... | $10.52^{+0.06}_{-0.05}$ | $10.65^{+0.07}_{-0.06}$ |
| | EM[†]$[\times10^{18}{\rm cm}^{-5}]$.. | 0.93±0.04 | 0.71±0.03 |
| | Surface brightness[§] | $1.1\times10^{-13}$ | $0.9\times10^{-13}$ |
| VNEI (ejecta) | $kT_{\rm e}$[keV] ......... | 0.50±0.01 | 0.55±0.01 |
| | O(=N) .......... | 0.52±0.04 | 2.6±0.2 |
| | Ne .............. | 0.27±0.03 | 0.9±0.1 |
| | Mg ............. | 0.43±0.04 | 1.5±0.1 |
| | Si .............. | 1.8±0.1 | 8.8±0.3 |
| | S .............. | 2.9±0.5 | 9.3±1.2 |
| | Fe .............. | 0.68±0.02 | 2.36±0.07 |
| | $\log(\tau/{\rm cm}^{-3}\,{\rm sec})$.... | 11.12±0.03 | 11.32±0.02 |
| | EM[†]$[\times10^{18}{\rm cm}^{-5}]$.. | 0.65±0.01 | 0.15±0.003 |
| | Surface brightness[§] | $1.0\times10^{-13}$ | $0.69\times10^{-13}$ |
| Power-law | Photon Index...... | 1.4±0.1 | 1.5±0.2 |
| | Norm[‡] .......... | 3.9±0.7 | 2.9±0.6 |

**Fig. 5.** EM profiles as a function of radius. Our data are shown with circles for E rim or triangles for NW rim. The solid or dashed lines are the best-representative models for E rim and NW rim, respectively. We set the radius of the SNR to be $R = 48'$ ($4.3 \times 10^{19}$ cm at a distance of $1\,\text{kpc}$) which is derived from the ROSAT PSPC surface brightness contour.

(NW). This fact suggests that the forward shock is not propagating into a uniform ambient density, but recently encountered a denser material than the shock had propagated before. The gradual increase of $\tau$ toward the shock front (see, Table 1 or Table 2) also supports the idea that the forward shock is now encountering a denser material.

Even if the SNR is not explained by a simple Sedov solution, we can estimate the age of the SNR by applying a simple Sedov solution in a uniform ambient density. Then, the age is calculated to be $11000 \ (T_s/0.3\,\text{keV})^{-0.5}(R/50')(d/1\,\text{kpc})$ yr. Considering that the forward shock is now encountering a denser material, the age from the simple Sedov solution would be an upper limit of the age of the SNR.

We found possible evidence that the forward shock is now interacting with a denser material which surrounds the SNR. A candidate for the denser material is indeed found around G156.2+5.7 as an HI shell surrounding this SNR (Reich et al. 1992). Therefore, the pre-shock ambient density of $\sim 0.09\,\text{cm}^{-3}$ derived by the comparison with a simple Sedov profile must be an upper limit for the density inside the denser material. In this context, the SN explosion which produced G156.2+5.7 occurred in a very low-density (less than $0.09\,\text{cm}^{-3}$) medium. The low density is reasonably expected to be a cavity evacuated by a stellar wind of the progenitor star. On the other hand, the relatively dense material that the forward shock is now encountering is suggestive to a wall of the cavity.

A powerful method to estimate the mass of the progenitor star is to compare relative metal abundances measured for the ejecta with those expected in nucleosynthetic models. We successfully measured the metal abundances of the ejecta, eliminating the contamination from the swept-up ISM along the line of sight by using a two- (i.e., the ISM and the ejecta) component VNEI model. Figure 6 shows the comparison of several metal abundances relative to O between our data and various nucleosynthetic models. Here, we take the metal abundances measured in
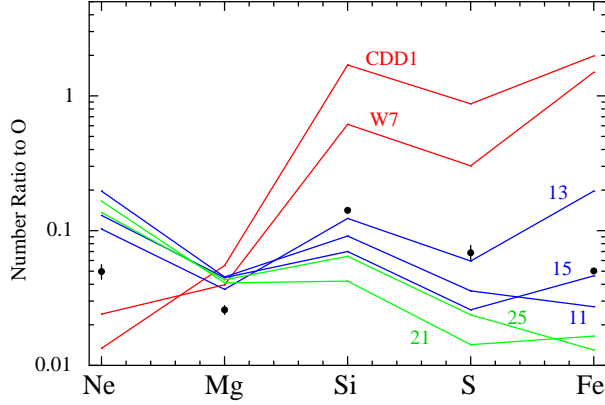
14

**Fig. 6.** Metal abundances of Ne, Mg, Si, S, and Fe to O. Our data are those derived for the ejecta component at the surrounding region in the central FOV. Red solid lines are those expected in Type-Ia (CDD1 or W7) models (Iwamoto et al. 1999). Blue lines are those expected in core-collapse models from relatively low-mass progenitors (11 $M_\odot$ [Woosley & Weaver 1995]; 13 $M_\odot$ [Thielemann et al. 1996]; 15 $M_\odot$ [Rauscher et al. 2002]). Green lines also represent core-collapse models but from relatively high-mass progenitors (Rauscher et al. 2002).

the surrounding region in the central FOV as the representative ejecta abundances. We employ Type-Ia models from Iwamoto et al. (1999), while core-collapse models with progenitor masses of 11 $M_\odot$ from Woosley & Weaver (1995), 13 $M_\odot$ from Thielemann et al. (1996), 15 $M_\odot$, 21 $M_\odot$, and 25 $M_\odot$ from Rauscher et al. (2002). We then find that our data prefer core-collapse models with relatively low-mass progenitors (below 15 $M_\odot$) for the origin of G156.2+5.7. However, we should note that the metal abundances of the ejecta are determined in a very limited region of G156.2+5.7. In order to determine the metal abundances for total ejecta, we need further X-ray observations of G156.2+5.7.

The HI shell surrounding G156.2+5.7 is possible evidence of the wall of the cavity as already suggested by Reich et al. (1992). If this HI shell is indeed the wall of the cavity, the radius of the cavity is estimated to be ∼15 ($d$/1 kpc) pc (i.e., the radius of the SNR). McKee et al. (1984) calculated the size of a cavity created by a massive star of type earlier than B0 (∼15 $M_\odot$) to be a radius of 50 pc. Within the range of the distance (1–3 kpc) to G156.2+5.7, the radius of the cavity is lower than 50 pc. Therefore, the relatively small size of the possible cavity also supports that the progenitor star of G156.2+5.7 is less massive than 15 $M_\odot$.

*4.2.   Non-Thermal Emission*

In the NW rim, the non-thermal emission comes from just behind the forward shock (see, Table 2). This suggests that the non-thermal emission originates from the relativistic electrons accelerated by the forward shock. Then, we should note that the value of $kT_e$ just behind the forward shock is derived to be about 0.3 keV, which results in a shock velocity of ∼500 $(kT_e/0.3\,\mathrm{keV})^{0.5}$ km sec$^{-1}$ assuming thermal equilibration between ions and electrons. The assumption seems to be reasonable, since the the expected proton temperature, ∼0.2

**Table 4.** Spectral-fit parameters derived by the SRCUT model.

| Parameter | NW1 | NW2 | NW3 | Ellipse | Surrounding |
|---|---|---|---|---|---|
| $\nu_{\rm rolloff}[\times 10^{16}{\rm Hz}]\ldots$ | $0.95\pm0.05$ | $1.28\pm0.04$ | $1.28\pm0.02$ | $1.63\pm0.09$ | $1.20\pm0.05$ |
| Surface brightness$^\dagger$ | $0.75\times10^{-14}$ | $1.2\times10^{-14}$ | $1.2\times10^{-14}$ | $0.69\times10^{-14}$ | $0.43\times10^{-14}$ |
| $\chi^2/{\rm d.o.f.}\ \ldots\ldots\ldots$ | $691/590$ | $1043/910$ | $972/797$ | $1315/1101$ | $1610/1332$ |

$^*$The errors are in the range $\Delta\chi^2 < 2.7$ on one parameter.

$^\dagger$In unit of ${\rm erg\,cm^{-2}\,sec^{-1}\,arcmin^{-2}}$ in a range of 0.5–10 keV.

$(\tau/6\times10^{10}\,{\rm cm^{-3}sec})^{-1}(kT_{\rm e}/0.3\,{\rm keV})^{2.5}\,{\rm keV}$, is comparable to the measured electron temperature. Although this equation is valid only for highly non-equilibrium stage of shocked plasma, the resultant value at least supports that thermal equilibrium is almost reached. In addition, we should note that the electron-proton thermal equilibration is expected in slower shocks (e.g., Rakowski 2005). It is surprising that we detect non-thermal X-ray emission from such a slow shock, since a currently accepted theory of diffusive shock acceleration requires high shock velocity of at least $2000\,{\rm km\,sec^{-1}}$ to produce non-thermal emission in the X-ray energy band. The slow shock might require unacceptably high efficiency of particle acceleration. Therefore, we check the validity of non-thermal origin for the hard-tail emission, based on morphologically and spectral features.

Regarding the morphology, relatively strong non-thermal radio emission is detected in the northern and the southern shell regions, while relatively weak emission is detected from the central portion of the remnant. Therefore, the distribution of the X-ray hard-tail emission matches the radio morphology; the X-ray hard-tail emission is detected with strong intensity in the NW rim, with weak intensity in the central portion, while it is not significantly detected in the E rim. This suggests that the radio emission and X-ray hard-tail emission have the same origin with each other, supporting the origin of the X-ray hard-tail emission is non-thermal synchrotron. In this context, we expect to detect non-thermal X-ray emission from the southern rim of the SNR, which will be checked by future X-ray observations.

To check spectral features in multi-wavelength emission, we introduce the SRCUT model, which describes synchrotron radiation from a power-law distribution of electrons with an exponential cut-off (Reynolds & Keohane 1999) instead of the power-law model. In this model, we fix the radio spectral index to 0.48 (Xu et al. 2007). The flux at 1 GHz is also fixed at the value determined by radio observations (based on figure 1 in Xu et al. 2007); $2.1\,{\rm mJy\,arcmin^{-2}}$ for the NW rim, $0.83\,{\rm mJy\,arcmin^{-2}}$ for the central portion. Thus, the only free parameter in the SRCUT model is the roll off frequency, $\nu_{\rm rolloff}$. In this way, we fit all the spectra in which we detected hard-tail emission. The measured roll off frequencies and $\chi^2$-values are summarized in Table 4. The fits are fairly good, although they are slightly worse than those derived by using the power-law model (see, Table 2 or Table 3). The measured roll off frequency, $\sim 1.5\times10^{16}$ Hz, is relatively low compared with those derived in young historical SNRs; $26\times10^{16}$Hz for Tycho

(Tamagawa et al. 2008), $20\times10^{16}$Hz for Kepler (Cassam-Chenaï et al. 2004), and $5.7\times10^{16}$Hz for SN1006 (Bamba et al. 2008). The low value of $\nu_{\mathrm{rolloff}}$ is in a sense that the efficiency of particle acceleration can be reduced. Now, we calculate the efficiency of particle acceleration. The roll off frequency is expressed as

$$\nu_{\mathrm{rolloff}} = 1.6 \times 10^{16}(B/10\mu\mathrm{G})(E_{\mathrm{max}}/10\mathrm{TeV})^2 \ \ \mathrm{Hz},$$

where $B$ is a strength of ambient magnetic field and $E_{\mathrm{max}}$ is a maximum energy of accelerated electrons (Reynolds 1998). Equating the synchrotron loss time to acceleration time, $E_{\mathrm{max}}$ is written down as follows (Uchiyama et al. 2003),

$$E_{\mathrm{max}} = 67(B/10\mu\mathrm{G})^{-0.5}(v_{\mathrm{s}}/2000\,\mathrm{km\,sec^{-1}})\eta^{-1/2} \ \ \mathrm{TeV},$$

where $v_{\mathrm{s}}$ is the shock velocity and $\eta$ is the so-called gyrofactor, i.e., the ratio of the particle mean free path to the gyroradius, and represents the efficiency of particle acceleration. Combining the above two equations, we can derive the following equation,

$$\nu_{\mathrm{rolloff}} = 7.2 \times 10^{17}(v_{\mathrm{s}}/2000\,\mathrm{km\,sec^{-1}})^2\eta^{-1} \ \ \mathrm{Hz}.$$

Substituting the measured $\nu_{\mathrm{rolloff}}$ of $1.5\times10^{16}$ Hz and the forward shock velocity of $500\,\mathrm{km\,sec^{-1}}$, we obtain the value of $\eta$ to be 48 (If thermal equilibration has not achieved yet behind the shock front, the shock velocity will be faster than $500\,\mathrm{km\,sec^{-1}}$ so that $\eta$ will be larger than 48). Thus, the particle acceleration is much less efficient than that taken place in the RXJ1713.7-3946 SNR, in which we see the extreme Bohm diffusion limit, $\eta = 1$ (Uchiyama et al. 2007). Therefore, the fact that the slow ($\sim500\,\mathrm{km\,sec^{-1}}$) shock in G156.2+5.7 produces non-thermal X-ray emission turns out to be acceptable from a theoretical point of view of diffusive shock acceleration. We consider that the detection of non-thermal X-ray emission associated with the slow shock in G156.2+5.7 is just simply because the flux ratio of non-thermal to thermal emission in this SNR is higher than those in the general middle-aged SNRs where non-thermal X-ray emission is not detected. Ellison et al. (2000) argued that a weak ambient magnetic field and/or a low ambient density yield the high flux ratio between non-thermal and thermal emission. As for the ambient density, we obtain similar ambient densities between the E rim ($0.093\,\mathrm{cm^{-3}}$) and the NW rim ($0.087\,\mathrm{cm^{-3}}$). However, we did not detect significant non-thermal emission from the E rim, but detected it only from the NW rim. Therefore, we suggest that the magnetic field plays an important role to the non-thermal/thermal flux ratio for the case of G156.2+5.7.

We discuss the nature of the central non-thermal emission in G156.2+5.7. The central bump isolated from both the northern and the southern shell in the radio image reminds us of a plerion for the nature of the central non-thermal emission, although there is no apparent counterpart of a pulsar/pulsar wind nebula. Xu et al. (2007) conclude that the emission from the central portion came from the shell of the SNR rather than a plerion because radio spectra do not show spectral flattening in the central portion of the remnant which is expected in the case of pulsar wind nebula. In principle, it is possible for the shell to be projected to the

center of the SNR. In the simulations of Orlando et al. (2007) to investigate the origin of the asymmetries in bilateral SNRs, we find such an example. In the paper, we find that the radio morphology of G156.2+5.7 is similar to the surface brightness of non-thermal emission expected in a situation that the bilateral radio limbs are parallel to the ambient magnetic field and a gradient of ambient density is perpendicular to the magnetic field (see figure 5 in Orlando et al. 2007). Although the possibility that the central non-thermal emission is a plerion can not be completely ruled out, it is preferred that the central non-thermal emission is associated with the shell of the SNR. Further X-ray observations around the central portion of the SNR will allow us to investigate a detailed variation of spectral index around the center of the SNR. If we see strong spectral variation, as is generally seen in pulsar wind nebulae (e.g., Petre et al. 2007), the origin would be most likely a plerion, otherwise the central non-thermal emission is associated with the shell of the SNR.

## 5. Conclusions

We have observed the middle-aged SNR G156.2+5.7 with the Suzaku satellite in three pointings which are targeted at the E rim and the NW rim, and the central portion of the SNR. Hard-tail X-ray emission is detected in the NW rim and the central portion, while it is not significantly detected in the E rim. The distribution of the hard-tail emission seems to be coincident with that of the radio non-thermal emission. Also, multi-wavelength emission is well represented by a so-called SRCUT model. These facts lead us to conclude that the hard-tail emission originates from non-thermal synchrotron emission. The velocity of the forward shock which likely produces the non-thermal X-ray emission in the NW rim is estimated to be $\sim 500 \, \mathrm{km \, sec^{-1}}$, assuming thermal equilibrium between ions and electrons. The shock might be the slowest among those having non-thermal emission in the X-ray wavelength. The relative abundances in the ejecta component suggests that the origin of G156.2+5.7 is a core-collapse SN explosion whose progenitor is a relatively low-mass star of $\sim 15 \, \mathrm{M_\odot}$.

## References

Anders, E., & Grevesse, N. 1989, Geochim. Cosmochim. Acta, 53, 197

Bamba, A., et al 2008, PASJ, 60, S153

Borkowski, K. J., Lyerly, W. J., & Reynolds, S. P. 2001, ApJ, 548, 820

Cassam-Chenaï, G., Decourchelle, A., Ballet, J., Sauvageot, J-L., Dubner, G., & Giacani, E. 2004, A&A, 427, 199

Cassam-Chenaï, G., Hughes, J. P., Ballet, J., & Decourchelle, A. 2007, ApJ, 665, 315

Ellison, D. C., Berezhko, E. G., & Baring, M. G., 2000, ApJ, 540, 292

Gerardy, C. L., & Fesen R. A. 2007, MNRAS, 376, 929

Hwang, U., Flanagan, K. A., & Petre, R. 2005, ApJ, 635, 355

Iwamoto, K., Brachwitz, F., Nomoto, K., Kishimoto, N., Umeda, H., Hix, W. R., & Thielemann, F. K., 1999, ApJS, 125, 439

Koyama, K. et al. 2007, PASJ, 59, S23

Laming, J. M. 2001, ApJ, 546, 1149

Levenson, N. A.. & Graham, J. R. 2005, ApJ, 622, 366

McKee, C. F., van Buren, D., & Lazareff, B. 1984, ApJ, 278, L115

Miller, E. D., et al. 2008, PASJ, 60, S95

Miyata, E., & Tsunemi, H. 1999, ApJ, 525, 305

Mitsuda, K., et al. 2007, PASJ, 59, S1

Orlando, S., Bocchino, F., Reale, F., Peres, G., & Petruk, O. 2007, A&A, 470, 927

Petre, R., Hwang, U., Holt, S. S., Safi-Harb, S., & Williams, R. M. 2007, ApJ, 662, 988

Pfeffermann E., Aschenbach B., & Predehl P., 1991, A&A, 246, L28

Rakowski, C. E. 2005, Adv. Space Res., 35, 1017

Rauscher, T., Heger, A., Hoffman, R. D., & Woosley, S. E. 2002, ApJ, 576, 323

Reich W., Fuerst E., & Arnal E. M. 1992, A&A, 256, 214

Revnivtsev, M., Molkov, S., & Sazonov, S. 2006, MNRAS, 373, L11

Reynolds, S. P. 1998, ApJ, 493, 375

Smith, R. K., Brickhouse, N. S., Liedahl, D. A., & Raymond, J. C. 2001, ApJL, 556, L91

Sugizaki, M., Mitsuda, K., Kaneda, H., Matsuzaki, K., Yamauchi, S., & Koyama, K. 2001, ApJS, 134, 77

Tamagawa, T. et al. 2008, PASJ, in press

Tawa, N., et al. 2008, PASJ, 60, S11

Tawa, N. 2008, PhD thesis (Osaka University)

Thilemann, F-K., Nomoto, K., & Hashimoto, M. 1996, ApJ, 460, 408

Uchiyama, Y., Aharonian, F. A., & Takahashi, T. 2003, A&A, 400, 567

Uchiyama, Y., Aharonian, F. A., Tanaka, T., Takahashi, T., & Maeda, Y. 2007, Nature, 449, 576

Yamauchi, S., Ueno, S., Koyama, K., Nomoto, S., Hayashida, K., Tsunemi, H., & Asaoka, I. 1993, PASJ, 45, 795

Yamauchi S., Koyama K., Tomida H., Yokogawa J., & Tamura K., 1999, PASJ, 51, 13

Woosley, S. E., & Weaver, T. A. 1995, ApJS, 101, 181

Xu, J. W., Han, J. L., Sun, X. H., Reich, W., Xiao, L., Reich, P., & Wielebinski, R. 2007, A&A, 470, 969